Challenges in Modulation Doping of MoO_3 on Hydrogen Terminated Diamond with HfO_2 Interfacial Layer

by

Aditya Vilasrao Deshmukh

A Thesis Presented in Partial Fulfillment
of the Requirements for the Degree
Master of Science

Approved February 2024 by the
Graduate Supervisory Committee:

Robert J. Nemanich, Chair
Terry Alford
Sui Yang

ARIZONA STATE UNIVERSITY
May 2024

ABSTRACT

Diamond transistors are promising as high-power and high-frequency devices having higher efficiencies than conventional transistors. Diamond possesses superior electronic properties, such as a high bandgap (5.47 eV), high breakdown voltage (>10 MV cm^{-1}), high electron and hole mobilities [4500 and 3800 $cm^2\ V^{-1} \cdot s^{-1}$, respectively], high electron and hole saturation velocities (1.5×10^7 and 1.05×10^7 cm s^{-1}, respectively), and high thermal conductivity [22 W $cm^{-1} \cdot K^{-1}$], compared to conventional semiconductors. Reportedly, the diamond field-effect transistors (FETs) have shown transition frequencies (f_T) of 45 and 70 GHz, maximum oscillation frequency (f_{max}) of 120 GHz, and radiofrequency (RF) power densities of 2.1 and 3.8 W mm^{-1} at 1 GHz. A two-dimensional-hole-gas (2DHG) surface channel forms on H-diamond by transfer doping from adsorbates/dielectrics in contact with H-diamond surface. However, prior studies indicate that charge transfer at the dielectric/ H-diamond interface could result in relatively low mobility attributed to interface scattering from the transferred negative charge to acceptor region.

H-terminated diamond exhibits a negative electron affinity (NEA) of -1.1 to -1.3 eV, which is crucial to enable charge transfer doping. To overcome these limitations modulation doping, that is, selective doping, that leads to spatial separation of the MoO_3 acceptor layer from the hole channel on H-diamond has been proposed. Molybdenum oxide (MoO_3) was used as dielectric as it has electron affinity of 5.9eV and could align its conduction band minimum (CBM) below the valence band maximum (VBM) of H-terminated diamond. The band alignment provides the driving potential for

charge transfer. Hafnium oxide (HfO_2) was used as interfacial layer since it is a high-k oxide insulator (~25), having large Eg (5.6 eV), high critical breakdown field, and high thermal stability. This study presents photoemission measurements of the electronic band alignments of the MoO_3/HfO_2/H-diamond layer structure to gain insight into the driving potential for the negative charge transfer and the location of the negative charges near the interface, in the HfO_2 layer or in the MoO_3 layer. The diamond hole concentration, mobility, and sheet resistance were characterized for MoO_3/HfO_2/H-Diamond with HfO_2 layers of 0, 2 and 4 nm thickness.

DEDICATION

To the vibrant future of semiconductor industry

ACKNOWLEDGEMENT

I am deeply grateful for the support and guidance I have received throughout my research journey and the completion of this thesis. Foremost, my heartfelt thanks go to my advisor and committee chair, Dr. Robert Nemanich. His unwavering mentorship and support have been pivotal. Joining Dr. Nemanich's research group not only gave me comfort and confidence but also significantly contributed to the success of my academic pursuits. I am profoundly appreciative of his patience, guidance, and expertise, which have been crucial in shaping and realizing this research.

My gratitude extends to the esteemed members of my committee, Dr. Terry Alford, and Dr. Sui Yang, for their invaluable support and insightful guidance. Special thanks to Avani, whose assistance was instrumental in integrating me into this exceptional research group. Dr. Kevin Hatch deserves acknowledgment for enriching my understanding from fundamental concepts to complex project applications.

I am thankful to Gabriel for his valuable research input and assistance with equipment, and to Ali for his unwavering moral support. Parker's presence made the lab a more enjoyable environment. Franz Koeck's contributions during lab meetings were invaluable in troubleshooting and problem-solving. Dr. Leila Pashazanusi's guidance during my INTEL job interview process and her encouragement to aim higher have been greatly inspiring. Acknowledgment is also due to my new lab mates, Sahadat and Rajesh, for their kindness, and the Core facility and MTW staff members Xan, Jovan, Jaime, and Anthony for their assistance. My friends Mahie and Sairaj have been a constant source of well-being checks,

and my two closest friends at ASU, Mukesh, and Melike, have been steadfast support through every challenge.

Special thanks to Alan for fostering my resilience, and to my gym trainer Ronnie, an integral part of my life. Kirk and Carrie have been like American parents to me, always ready to lend an ear during tough times. My roommates deserve thanks for making home life smoother and more enjoyable. I'd also like to express my appreciation to James, whose company has been a delightful escape.

Most importantly, my family has been the cornerstone of my life. Their selfless love and the sacrifices they have made for my education and dreams have been the driving force behind everything I have achieved. I am eternally grateful for their unending support. In conclusion, I express my profound gratitude to the Department of Energy for their generous support via the ULTRA EFRC, under grant DE-SC0021230, which facilitated the growth of dielectric layers. Additionally, my sincere thanks go to the National Science Foundation for their financial backing through grant DMR-2003567, enabling the characterization of interfaces. This thesis is not only a reflection of my efforts but also a testament to the collective support and encouragement of everyone mentioned.

TABLE OF CONTENTS

CHAPTER Page

LIST OF FIGURES

Figure Page

Figure Page

LIST OF TABLES

Table Page

CHAPTER 1

INTRODUCTION

1.1 Diamond

The carbon allotrope diamond possesses a remarkable amalgamation of properties, making it an ‘extreme ’ material, highly appealing for a wide range of applications.[1] It possesses an extremely high thermal conductivity of up to 22 W/cm.K , while also being a bona fide electrical insulator in its intrinsic state due to a wide band gap of 5.4 eV.[2, 3] This results in an elevated breakdown field, approximately 13 MV/cm accompanied by substantial intrinsic carrier mobilities, with values recorded at 4500 $cm^2/V{\cdot}s$ for electrons and 3800 $cm^2/V{\cdot}s$ for holes, respectively.[4] Diamond has these unique properties due to the structure of its crystalline lattice.[5] Every carbon atom forms four sp^3-hybridised atomic orbitals, which overlap with neighboring atoms, establishing sigma (σ) bonds. This interaction leads to a compact C-C bond length of 0.154 nm and a robust bond energy of 711 kJ/mol. These robust covalent bonds facilitate the effective dissipation of heat through lattice vibrations, underlying diamond's exceptional intrinsic thermal conductivity, despite its significant bandgap and electrical insulation[6] This rare blend of high thermal conductivity and electrical resistance underscores diamond's distinctive suitability for advanced, high-power electronic applications.

Diamond's intrinsic durability makes it superior in extreme conditions relative to other materials. For example, in the 1970s, NASA utilized large-area natural diamonds as observation windows in their Venus space probes, capitalizing on diamond's resistance to the planet's highly corrosive atmosphere.[7]

Table 0.1: Comparison of Band Gap, electron mobility, relative dielectric constant, critical field, and thermal conductivity for popular semiconductor materials.

Semiconductor Material	**Band Gap (ev)**	**Electron Mobility μ cm^2/V-s**	**Relative Dielectric Constant ε**	**Critical Field E_c (kV/cm)**	**Thermal Conductivity σ_{th}**
GaAs	1.42	8500	13.1	400	55
GaN	3.4	900	9	3000	110
Ge	0.66	3900	16	100	58
Si	1.12	1400	11.7	300	130
GaP	2.26	250	11.1	1000	110
SiC (6H, α)	3.0	330	9.66	2400	700
SiC (4H, α)	3.2	700	9.7	3180	700
Diamond	5.4	1945	5.7	5700	2000

As Shown in Table 0.1, diamond distinguishes itself as a potentially superior semiconductor when compared to other materials like GaAs, GaN, Ge, Si, GaP, SiC. This superiority can be attributed to a unique combination of its exceptional properties, which are highly desirable in semiconductor applications, particularly for high-frequency, high-power electronics. Here is a comparative analysis explaining why diamond holds the potential to be the best semiconductor.

Mobility: Diamond exhibits high intrinsic carrier mobilities for both electrons and holes (4500 $cm^2/V \cdot s$ for electrons and 3800 $cm^2/V \cdot s$ for holes, as mentioned earlier)[4].While materials like GaAs and GaN also have high electron mobilities, diamond's balanced carrier mobility is beneficial for devices requiring both types of charge carriers.

Relative Dielectric Constant: Diamond has a relatively low dielectric constant, reducing parasitic capacitance in electronic devices. This is particularly advantageous in high-frequency applications where a low dielectric constant is essential for minimizing power loss and signal delay.

Critical Field: Diamond has an exceptionally high breakdown field (around 13 $MV/cm)^2$, significantly surpassing that of Si, GaAs, and even SiC. This high breakdown field allows for operation at much higher electric fields before the material becomes conductive, enabling devices that can handle higher voltages and power densities.

Thermal Conductivity: Diamond possesses the highest known thermal conductivity (22 $W/cm \cdot K$) among semiconductors. This property is crucial for heat dissipation, especially in high-power devices, as it helps in maintaining operational stability and prolonging the lifespan of electronic components.

Band Gap: With a wide band gap of 5.4 eV, diamond is an excellent electrical insulator until a significant amount of energy is provided. This wide band gap is beneficial for high-temperature and high-power applications, as it allows devices to operate at higher temperatures and voltages without suffering from leakage currents.

Today, the emergence of synthetic diamond through high-temperature, high-pressure (HPHT) or chemical-vapor deposition (CVD) methods has facilitated the creation of materials with controllable properties. Owing to its distinctive intrinsic characteristics, diamond has garnered considerable interest as a sturdy electronic material, particularly for applications in high-frequency and high-power electronics.

Table 0.2: Comparison of figures-of-merit for diamond compared with other semiconductors based on Baliga's analysis [8,9,10]

	Si	SiC	GaN	Diamond
Baliga FOM ($\varepsilon_r \mu_e E_{max}^3$)	1	440	2950	4.73×10^5
Baliga High Frequency FOM ($\mu_e E_{max}^2$)	1	58	237	1.2×10^4

Various figures of merit (FOMs) serve as crucial tools for evaluating the intrinsic potential of novel material systems across a spectrum of electronic applications(Table 0.2) Among these, the Baliga Figure of Merit (B_{FOM}), along with its high-frequency counterpart (BH_{FOM}) stands as a widely utilized metric.[9] The B_{FOM} is a ratio between the square of the avalanche breakdown voltage (V_B^2) and the specific on-state resistance for a device (Ron, sp). In terms of elementary material properties, B_{FOM} is often expressed as: $\varepsilon_r \mu_e E_{max}^3$where E_{max} is the critical electric breakdown field, μ_e is the electron mobility and ε_r is the electric permittivity of the semiconductor.

B_{FOM}'s cubic dependence on E_{max} discriminates in favor of high breakdown-field materials such as diamond. However, variations in E_{max} and $\mu_e$with

temperature and impurity concentration make this advantage more controversial.[11] Additionally , B_{FOM} assumes power losses are due to dissipation during a device's on-state operation, from current flow through the device's network of resistances. Hence, B_{FOM} is more valid to low frequency operation where conduction losses are dominant. The BH_{FOM} modifies this assumption by including the impact of switching losses due to the charging and discharging of the input capacitance resulting in an expression of power loss inversely proportional to $\mu_e E_{max}^2$, i.e. with a quadratic (and not cubic) dependence on E_{max}. Baliga's figures presented in Table 2 are adjusted to a relative scale, with silicon assigned a nominal value of 1. As shown in Table 0.2 intrinsic (or unintentionally doped) diamond outstrips other established wide-bandgap semiconductors.

Nevertheless, such comparative analyses based on figures of merit should be regarded as indicative assessments of a material's potential, relying solely on its intrinsic characteristics. For instance, devices fabricated from diamond have not yet achieved carrier mobilities that mirror those predicted by intrinsic material properties, underscoring the challenges encountered in the nascent stages of diamond semiconductor development. These challenges are inherent to the material's system; notably, the strong σ-bonding among carbon atoms in the diamond lattice renders substitutional doping a formidable task.

In contrast, surface transfer doping emerges as a viable alternative, circumventing the intrinsic barriers posed by traditional doping methods and unlocking the semiconducting potential of diamond. Although the detailed mechanisms of surface transfer doping remain under active investigation, substantial experimental progress over

the past decade has markedly deepened our comprehension of this unique characteristic of diamond. This advancement holds promise for leveraging diamond's exceptional properties in semiconductor applications, highlighting the dynamic evolution of our understanding and utilization of this material.

1.2 Challenges in developing mature doping process

Diamond, valued for its superior properties, has been extensively explored for electronic device applications. To exploit diamond's full potential, doping is essential to introduce a high and stable density of mobile charge carriers. However, developing a mature doping process for diamond has been challenging. Similar to other wide-bandgap semiconductors, achieving shallow donors and deep-level acceptors in diamond through impurity doping, with activation energies suitable for room-temperature operation, is particularly challenging. Boron has been the preferred impurity for achieving p-type doping in diamond, despite its considerable activation energy of 0.37 eV.[12] However, the relatively high ionization energy of boron in diamond often leads to degenerate doping levels, rendering the material semi-metallic and facilitating variable range hopping conduction.[13]

In high-quality, intrinsic, or lightly boron-doped diamond, researchers have observed hole mobilities (μ_h) around 2200 $cm^2/V{\cdot}s$.[5] However, in boron-doped diamond, mobility (μ_h) significantly diminishes with rising dopant concentrations or temperatures. At higher temperatures, the reduction in mobility is chiefly attributed to phonon-scattering mechanisms. [14], [15] Near room temperature, acoustic phonon scattering predominantly leads to a decrease in mobility, roughly following a $T^{-1.5}$ trend between 300

and 350 K. [16]Above 400 K, μ_h sharply declines following a $T^{-2.5}$ to $T^{-3.66}$ trajectory, due to the influence of additional optical phonon scattering.[14,15,17] Additionally, neutral impurity scattering plays a notable role in highly boron-doped diamond, where the deep-level ionization energy of boron results in holes being localized at the acceptor level, maintaining most impurities in a neutral state.[17] This degradation of hole mobility with increased carrier concentration and elevated temperatures detracts from the suitability of boron-doped diamond as a substrate for high-temperature electronic applications. Ion-implantation, a high-energy boron doping technique, often leads to significant lattice damage in diamond, compromising substrate quality and hindering device fabrication.[18] To circumvent this, boron incorporation typically occurs during growth. However, heavy boron doping in this phase can adversely affect growth rates and result in soot formation. Achieving a balance between high boron concentration ($>10^{20}$ cm^{-3}) and preserving the desired crystalline structure remains a substantial challenge.[19]

1.3 Hydrogen Termination on Diamond

In 1989, Landstrass and Ravi first reported the low electrical resistivity of H-terminated chemical vapor deposition (CVD) diamond surfaces with a surface conductivity of 10^{-6}-Ω^{-1} cm^{-1}, without any form of intentional impurity doping. [20]

Surface conductivity observed in H-terminated diamond, exhibiting sheet resistances ranging from 10^3 to 10^4 Ω/sq, is attributed to p-type carriers. These carriers have a sheet hole concentration of approximately 10^{13} /cm^2 and demonstrate hole mobilities between 10 and 100 $cm^2/V{\cdot}s$. To account for this p-type surface conductivity, multiple theoretical models have been explored. These include the passivation of deep levels by subsurface

hydrogen, creating a more conducive surface environment, and the generation of shallow acceptor states due to hydrogen incorporation within the lattice, both of which significantly influence the electronic structure of the surface.[20, 21,22] Additional models consider surface oxidation by adsorbed molecules, which alters the surface electronic states, and a charge transfer redox reaction within an adsorbed water layer, suggesting an interaction between the diamond surface and environmental factors[23,24].Another perspective is offered by the spontaneous polarization model, which posits an inherent polarization at the surface influencing conductivity. [25]Among these, the electrochemical surface transfer doping model has gained prominence and is currently regarded as the most accurate in explaining the observed conductivity. This model effectively combines the understanding of surface chemistry with electronic properties, offering a comprehensive explanation of the conductivity mechanisms in H-terminated diamond.[26],[27]

1.4 Diamond FETS

The development of Hydrogen-terminated diamond Field-Effect Transistors (H-diamond FETs) represents one of the most prominent applications of surface transfer doping in diamond technology. The two-dimensional hole gas (2DHG) formed by the transfer-doped H-diamond surface is ideally suited for creating planar electronic devices. This approach was first successfully demonstrated by Kawarada et al. in 1994, marking a significant milestone in the use of diamond-based materials for electronic device fabrication.[28] Figure 0.1 depicts an exemplary 3-terminal FET device by Kawarada et al., featuring a Chemical Vapor Deposition (CVD) grown H-diamond (100) substrate. This substrate undergoes transfer doping through air exposure and is equipped with an Aluminum gate contact and Gold source and drain ohmic contacts. The hydrogen

termination of the diamond surface not only enables the surface transfer doping process but also significantly diminishes the interface state density. This reduction allows for an unpinned surface that is responsive to the metal work-function, enhancing the device's overall performance.

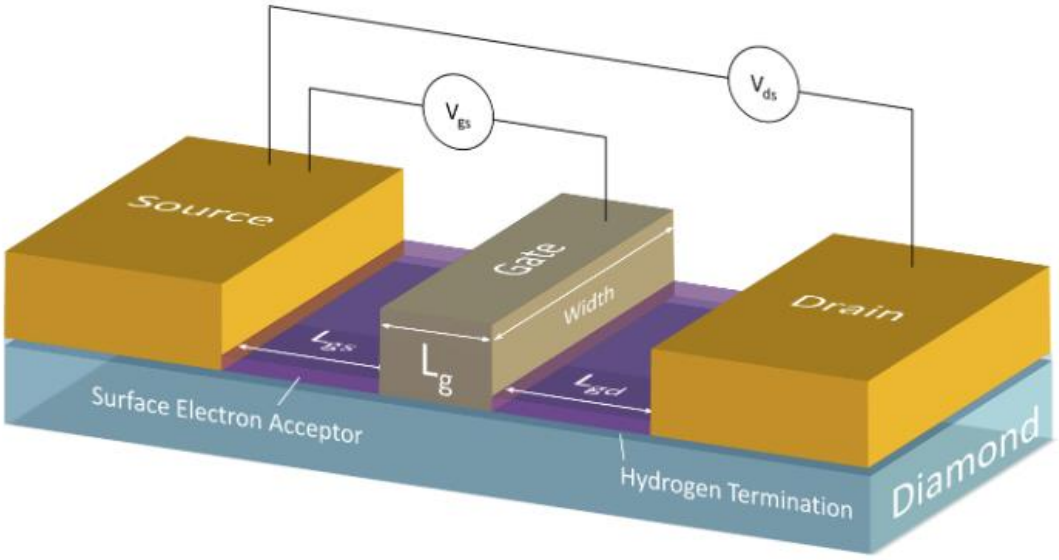

Figure 0.1 Illustration of a 3-terminal hydrogen-terminated diamond-based field effect transistor device, consisting of a source, drain and gate. Notable dimensions are represented, such as gate length (L_g), gate-source separation (L_{gs}) and gate-drain separation (L_{gd}). Reprinted from Crawford, et. al.[29]

Figure 0.1 illustration of a 3-terminal hydrogen-terminated diamond-based field effect transistor device, consisting of a source, drain and gate. Notable dimensions are represented, such as gate length (L_g), gate-source separation (L_{gs}) and gate-drain separation (L_{gd}). Figure 0.1 is adapted from Crawford, et. al.[29] By selecting metals with appropriate work functions, both Schottky and ohmic contacts can be effectively formed on the

resulting 2DHG in H-diamond FETs. This process involves using metals with low and high work functions for Schottky and ohmic contacts, respectively, and does not require thermal treatment for implementation. In this device configuration, with a gate length of 10 μm operating in enhancement mode, performance metrics included a maximum drain current of 1.6 mA/mm and an extrinsic transconductance reaching up to 200μS/mm.[28] This groundbreaking work confirmed the feasibility of utilizing transfer-doped H-diamond in surface-bound electronics, showcasing its potential in the field. Since its initial demonstration, advancements in H-diamond FET design, particularly through reducing gate length (L_g), have markedly enhanced device performance. Shorter Lg boosts the cut-off frequency (f_T) and maximum oscillation frequency (fmax), while a smaller overall source-drain distance ($L_{gs} + L_g + L_{gd}$) reduces the on-resistance (Ron). Conversely, a longer L_{gd} enhances off-state breakdown voltage by diminishing electric field concentration near gate and drain contacts. Additionally, a larger L_g can substantially improve off-state performance and power handling. Achieving low resistance contacts to the 2DHG in H-diamond is vital for high-performance FETs, especially influencing the R_{on} in current flow between source and drain. Contrary to FET devices that utilize Schottky-based gate contacts, where a low work-function metal directly contacts the H-diamond surface, significant efforts have been made in developing Metal-Oxide-Semiconductor FET (MOSFET) H-diamond devices. These devices integrate various dielectric materials beneath the gate metal, aiming to enhance the breakdown voltage potential and minimize current leakage through the gate contact.

1.5 Surface Conductivity of Diamond with Metal Oxides

To enhance the stability of surface conductivity in H-terminated diamond, a variety of solid encapsulation materials have been investigated, with metal oxides emerging as the most effective. Certain transition metal oxides (TMOs) have shown exceptional efficacy as transfer dopants for H-diamond, attributed to their high electron affinity (EA). TMOs possessing an EA greater than 4.3 eV, such as MoO_3, V_2O_5, and WO_3, are particularly effective, as their conduction band minimum (CBM) is positioned below the valence band maximum (VBM) of H-terminated diamond. This alignment facilitates enhanced carrier concentrations in the diamond's two-dimensional hole gas (2DHG), a phenomenon first reported by Russell et al. in 2013 with the application of molybdenum trioxide (MoO_3), which increases the 2DHG carrier concentration by an order of magnitude [30]

The underlying band bending mechanism, which accounts for the formation of the 2DHG in the presence of high EA materials, is depicted in Fig. 8. This mechanism involves the CBM of the surface electron acceptor being lower than the VBM of H-diamond, leading to upward band bending as the Fermi levels equilibrate, and consequently, the creation of a 2DHG beneath the diamond surface. It is therefore expected that carrier concentration may scale with the relative magnitude of the surface acceptors' Electron Affinity Driven by the relative electron affinity of the surface acceptor layer, thermodynamically favorable charge transfer to the surface material results in upward band bending. The same band bending was reported on MoO_3 induced transfer doping of H-diamond, with carrier densities up to ~1×10^{14}/ cm^2 driven by the large EA of MoO_3.[31]

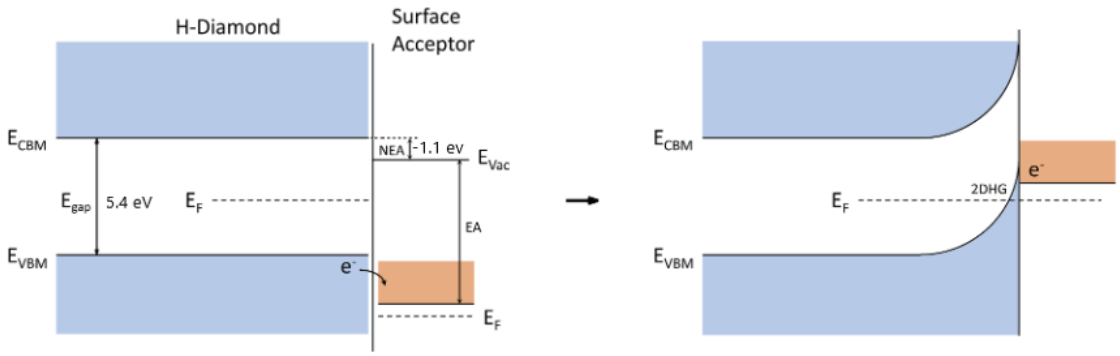

Figure 0.2 (Modified from Crawford, et. al.[29]) Energy Band Diagram Depicting 2D Hole Gas Generation in Hydrogen-Terminated Diamond via High Electron Affinity Material Contact.

Several other studies involving vanadium pentoxide (V_2O_5)[32] , tungsten trioxide (WO_3)[32], rhenium trioxide (ReO_3)[31], niobium pentoxide (Nb_2O_5)[32] and chromium trioxide (CrO_3)[33] were performed. Some of the lowest sheet resistances reported have been demonstrated by MoO_3, V_2O_5 and WO_3 with carrier densities in excess of 1×10^4/ cm^2.[31,32]. Transition Metal Oxides (TMOs) consequently emerge as a superior electron acceptor solution over molecular species like C_{60} or NO_2, owing to their enhanced stability over a broad temperature spectrum and their ability to produce consistently high carrier concentrations. This performance advantage is attributed to TMOs being solid materials with properties that can be precisely controlled.

But, the utilization of high electron affinity materials as acceptor layers introduces a challenge where the hole mobility diminishes as the hole concentration increases. This reduction in mobility is attributed to the nature of charge transfer doping, where the ion density is not evenly dispersed within the oxide but instead accumulates in a

layer adjacent to the hole accumulation layer in the diamond. Such an accumulation of ions near the hole accumulation layer leads to increased Coulomb scattering, adversely affecting the mobility of holes.

The degree of ionized impurity scattering, a pivotal consideration in this context, is correlated with the density of ionized impurities. Specifically, in charge transfer doping scenarios, the ion density within the adsorbate layer mirrors the hole sheet concentration in the diamond. Consequently, an elevation in the hole sheet concentration invariably results in diminished hole mobility, primarily due to the enhanced ionized impurity scattering. Moreover, this scattering mechanism, induced by ions in the adsorbate layer, significantly curtails the performance of electronic devices that rely on the surface conductivity of H-terminated diamond.

Moreover, Enhancing the thermal and chemical stability of diamond's surface conductivity is crucial for electronic device applications. Advancements in developing novel passivation layers are necessary to either stabilize existing adsorbates or provide effective alternatives.

In previous studies, gate dielectric materials used in the fabrication of hydrogen-terminated diamond-based field effect transistor devices were reported for Al_2O_3[34,35], SiNx[36], Y_2O_3 [37], V_2O_5[32], SiO_2[38], HfO_2[39], LaB_6[40] and MoO_3[41].

Device performance is significantly influenced by the dielectric properties, with the band gap and dielectric constant being paramount. The band gap is essential for the confinement of carriers within the diamond, whereas the dielectric constant influences the distribution of the electric field across the dielectric layer. Table 0.3 summarizes the band gaps,

dielectric constants, and band offsets of dielectrics commonly utilized on H-terminated diamond, providing a comprehensive overview essential for device optimization.

Table 0.3 Band Gap (E_g), dielectric constant (K), Conduction Band Offset (CBO), and Valence Band Offset (VBO) measured for dielectrics on H-Terminated Diamond. Modified from Yang, et. al.[42]

	MoO_3	V_2O_5	ZnO	ZrO_2	TiO_2	HfO_2	$LaAlO_3$	SiO_2	Al_2O_3
Eg	2.8	2.3	3.4	5.6	3.2	5.6	6.7	9.1	7.2
CBO	-5.9	-5.65	-3.85	-2.2	-4.9	-2.5 (2.3)	-2.8	1.5	-1.2
VBO	3.8	2.45	1.75	2.3	2.6	3.3 (2.6)	4.0	2.1	2.9
K	18	20	8	25	80	25	30	3.9	9

Among the dielectric layers listed before for H-diamond MOSFETs, Aluminum Oxide (Al_2O_3) stands out as the most thoroughly investigated and favored dielectric layer. Its application as both a gate dielectric and a channel passivation layer has markedly improved device performance and stability. A notable achievement includes attaining the highest drain current of 1.35 A/mm in an H-diamond FET, facilitated by a 400 nm gate length and Al_2O_3 passivation post-NO_2 exposure. [43]However, despite these advancements, Al_2O_3's high defect density and relatively low dielectric constant (9) have been points of concern. Yu Yang et al. have demonstrated that Al_2O_3 serves as an exceptional interfacial layer, enhancing FET mobility by an order of magnitude.[35] Yet, for the commercial viability of Diamond FETs, there are significant challenges to overcome. On the other hand, Hafnium Oxide, though less explored, is recognized for its lower defect density[44],[45], high dielectric constant[46],[47], and a bandgap[46,45] that rivals deposited Al_2O_3,

presenting a promising alternative for future research and development in Diamond FET technology.

Liu et al the deposited HfO_2 films using TALD technique at low temperature. The electrical properties of the ALD-HfO_2/H-diamond MOS diodes with the RTA treatment were investigated. The current density, J, of the MOS diode after annealing at 300 ^oC was as small as 10^{-8} A/cm^2 at the gate bias of -5.0 V. [39] Hence, the novelty of this research make it more challenging to comprehend.

In their pioneering work, Liu et al. deposited HfO_2 films on H-terminated diamond using the Thermal Atomic Layer Deposition (TALD) technique at low temperatures. This study delved into the electrical properties of ALD-HfO_2/H-diamond Metal-Oxide-Semiconductor (MOS) diodes, particularly after undergoing Rapid Thermal Annealing (RTA) treatment. Remarkably, the current density (J)of the MOS diode post-annealing at 300°C was measured to be as low as 10^{-8} A/cm^2 at the gate bias of -5.0 V

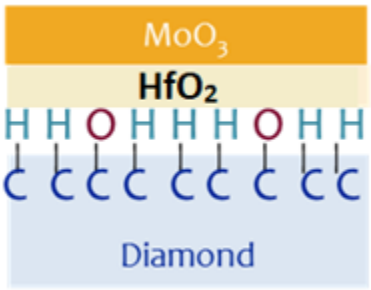

Figure 0.3 Structure of H-Terminated Substrate/ HfO_2 interfacial layer/ MoO_3 acceptor layer

The author aims to refine the fabrication process for the structure depicted in Figure 0.3 In the subsequent sections, we will delve into the fabrication challenges and the characterization techniques pertinent to this structure, providing a comprehensive overview of the optimization efforts undertaken.

Chapter 2

EXPERIMENTS

1.6 Substrate selection

A range of commercially obtained CVD-grown diamonds were utilized for distinct variations of the process. Initially, procedures involving both thermal ALD and Plasma Enhanced ALD for Hafnium oxide deposition employed optical grade 5×5 mm^2 type IIa CVD single crystalline undoped diamond (100) substrates, procured from EDP. However, charging shifts encountered during X-ray Photoelectron Spectroscopy (XPS) analysis necessitated a reconsideration of substrate choice.

To counteract the charging issues, the selection shifted to highly boron-doped polycrystalline 10×10 mm^2 type IIa diamond (100) substrates, sourced from Element Six (E6). While these highly doped substrates effectively mitigated the charging effects, they introduced a challenge: their bulk conductivity masked subtle variations in hole mobility, sheet concentration, and charge carrier dynamics. In essence, the overall conductivity obscured the localized surface charge transfer effects that were crucial for the study.

In the concluding series of experiments, the focus was placed on low boron-doped 5×5 mm^2 type IIa CVD single crystalline undoped diamond (100) substrates also sourced from Element Six (E6). These substrates struck a balance, providing sufficient conductivity to prevent charging while preserving the visibility of nuanced changes in surface charge dynamics. The boron-doped epitaxial layer on these substrates was precisely engineered in a plasma CVD system with components from iPlas Corp., ensuring meticulous control over the doping level and the integrity of the diamond surface.

This strategic selection of substrates was crucial for delving into the effects of Hafnium oxide as an interfacial layer in diamond semiconductor research, a field where such studies are still in their infancy. Selecting the optimal substrate was crucial, evolving from intrinsic to high, and then to low boron-doped substrates to fine-tune the balance. Despite thorough planning, pinpointing the exact impact of the Hafnium oxide layer remained a complex challenge, reflecting the intricate nature of this new interface. It highlights the necessity for ongoing, innovative exploration in this promising yet challenging field.

Subsequent processing steps for all samples were consistent, and the procedure for the Chemical Vapor Deposition (CVD) type IIa (100) substrates, sourced from EDP Corporation, will be detailed in the following paragraphs. This approach ensures uniformity across all samples and allows for a clear, methodical presentation of the experimental process.

1.7 Hydrogen Termination

Hydrogen termination was performed on CVD type IIa (100) substrates sourced from EDP corporation. The plates were specified as 5x5x0.3mm with (100) orientation and 2.5°±0.5° miscut. A hot wet-chemical clean was performed which included a boil in an acid mixture (H_2SO_4 /H_2O_2 /H_2O, 3:1:1) at 220 °C for 15 min and an HF treatment for 5 min. After each step, the plates were rinsed with DI water and after the final step dried with nitrogen gas.

A 0.5-inch diameter molybdenum disk was used as a sample holder, the assembly was loaded into the CVD reactor, and the chamber evacuated to a pressure in the

low 10-8 Torr. The plasma-assisted chemical vapor deposition system (PECVD) was solely used for the growth of intrinsic diamond and thus presented a clean processing ambient. The PECVD system utilized an ASTeX 5250 reactor and was equipped with a custom built, water-cooled sample stage. A 1.8kW MKS microwave source was used for plasma ignition whereas an auto-tuner adjusted the reflected microwave power. Gas flow was controlled by mass flow controllers (MFC's), and the pressure measured via a Baratron capacitance gauge. The base pressure was achieved by a turbomolecular pump backed by a roots pump. For processing an Edwards iQDP40 positive displacement pump was used. All pumping was oil free to avoid contamination from back streaming vapors. After the base pressure was achieved by the turbo-pump, the chamber was flushed with research grade hydrogen for 10min.

To ignite the hydrogen plasma, a gas flow of 400sccm was established, and the pressure was increased to 5 Torr. A stable discharge was established at an initial microwave power of 180W. For the actual hydrogen passivation, the pressure was then increased to 60-65Torr, and the microwave power adjusted to about 1100W. The temperature of the substrate was acquired by a dual-wavelength (2.1/2.4μm) Wiliamson Pro DW-24-40-C-FOV optical pyrometer where the circular field-of-view region was focused on the sample surface. Reactor pressure and microwave power were adjusted to achieve a substrate temperature of 800-850°C. The sample/sample holder assembly utilized plasma focusing where selective heating of the substrate was achieved as shown in Figure 0.1 This approach allowed a clean processing ambience as no hot spots in the chamber were established from where thermal desorption processes could contaminate the passivation process. The hydrogen passivation was then performed for 10min. To maintain

the hydrogen passivated surface a progressive cool-down was performed where the surface temperature dropped to <475°C within 7sec. After the cool-down the reactor was vented with argon gas and the samples removed.

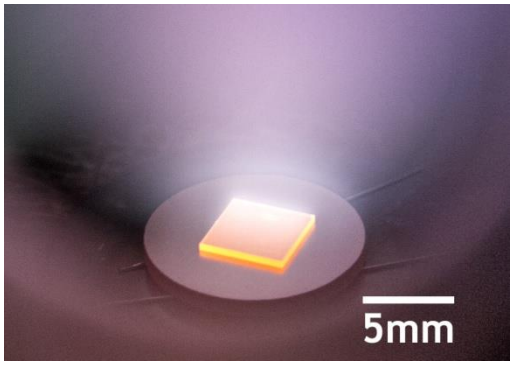

Figure 0.1 View into the PECVD reactor during hydrogen passivation with selective heating of the square diamond plate (Picture credit: Franz Koeck)

1.8 Boron Epitaxial Growth

For the last set of samples (type IIa CVD single crystalline undoped diamond (100) substrates) Boron-doped diamond films were grown by microwave (2.54 GHz) plasma enhanced CVD in a stainless steel, high-flow reactor. Diamond deposition was preceded by substrate cleaning using H_2 plasma excited with 1200 W microwave power for 5 min at a substrate temperature of 850 °C. Chamber pressure was maintained at 15 Torr throughout deposition with a CH_4 (99.999% purity, Matheson) flow rate of 4.0 standard cubic centimeters per minute (sccm), and H_2 (99.999% purity, Matheson) flow rate of 396 sccm. A boron concentration of ~5×10^{17} cm^{-3} resulted from residual boron in the deposition chamber, originating from trimethyl boron gas mixture in H_2 (3% by volume, Airgas)

1.9 ALD Processes

1.9.1 Plasma Enhanced Atomic Layer Deposition (PE-ALD)

Hafnium oxide (HfO_2) films were deposited using a remote Plasma Enhanced Atomic Layer Deposition (PEALD) technique for last 3 sets of substrates (intrinsic EDP SCD (100), Highly boron doped PCD, and low boron doped E6 SCD substrate.

Tetrakis[(EthylMethyl)Amido]Hafnium[$(EtMe)N]_4Hf$, commonly referred to as TEMAH, served as the metal precursor, with oxygen plasma acting as the oxidant precursor. The metal precursor was stored in a stainless-steel bubbler, encased in a heating jacket. This arrangement maintained the precursor at a constant 75°C, ensuring sufficient vapor pressure for the vapors to be efficiently delivered to the bypass valve via a vapor-drawn mechanism. Argon, employed as the carrier gas, facilitated the transport of the metal precursors to the deposition chamber. Simultaneously, oxygen plasma was generated by a radiofrequency (rf) source, delivering 30 W at 13.56 MHz, and was directed through a helical copper coil wrapped around a quartz tube, approximately 32 mm in diameter, positioned roughly 10 inches above the substrate. This setup ensured the efficient generation and delivery of the highly reactive oxygen species necessary for the ALD process.

Preceding the deposition process, the substrates were subjected to an annealing step at 300°C for 10 minutes. This step was crucial for eliminating adsorbed atmospheric impurities.

To provide a comprehensive understanding of the deposition process, the Table 0.1 below delineates the specific gas flow rates and pulse durations for the gases involved:

Table 0.1 Gas flow rates and pulse durations for the ALD growth of hafnium oxide

	Flow Rate (sccm)	Pulse time (sec)
Argon (Ar)	40	1
Oxygen (O_2)	35	10
Nitrogen (N_2)	40	50

The specific flow rates and pulse timings for Argon, Oxygen, and are precisely calibrated to optimize the deposition process, ensuring precision and uniformity in the film growth. Each component of the gas flow and pulse timing plays a crucial role in the ALD process: Argon flow rate of 40 sccm ensures a steady and controlled delivery of the precursor, preventing any excessive or insufficient supply that could lead to uneven film growth. The short pulse time of 1 second is sufficient to introduce the precursor into the chamber without causing oversaturation.

Oxygen flow rate of 35 sccm is optimized to supply an adequate amount of oxygen for the reaction, ensuring complete and uniform oxidation without excess that could lead to unwanted reactions or byproducts. The longer pulse time of 10 seconds for oxygen allows for thorough interaction between the oxygen plasma and the metal precursor on the substrate's surface. This ensures complete and uniform formation of the HfO_2 film across the substrate.

Nitrogen is utilized as a purging gas in this ALD process. The flow rate of 40 sccm and relatively long pulse time of 50 seconds ensures that the chamber is thoroughly purged,

preventing any cross-contamination between cycles. This is crucial for maintaining the purity and uniformity of the HfO_2 films.

1.9.2 Thermal Atomic Layer Deposition (TALD)

Deposition of Hafnium oxide (HfO_2) films with thicknesses of 2 nm, 4 nm, and 8 nm was carried out at Arizona State University's Nano-fab facility using the Cambridge Savannah Thermal Atomic Layer Deposition system. Hydrogen-terminated single-crystal diamond (SCD) substrates were pre-annealed at 300 °C to remove surface adsorbates, ensuring a clean surface for the subsequent deposition process. The growth rate was maintained at 0.9 nm per cycle, employing water (H_2O) as the oxidizing agent, in contrast to the O_2 plasma used in Plasma Enhanced ALD processes. The deposition itself was conducted at 180 °C. The precise measurement of film thickness was achieved using in-situ Woollam ellipsometry, based on Cauchy's model.

1.10 Hydrogen Plasma Treatment to regenerate surface charge and heal HfO_2 film

Upon the completion of Hafnium oxide (HfO_2) deposition, the substrate surface underwent a hydrogen plasma post-deposition treatment for 15 minutes at an approximate temperature of 350°C, which was monitored using a pyrometer to ensure thermal stability. The chamber pressure during this phase was regulated to 100 mTorr, with a hydrogen gas flow maintained at 20 sccm. This flow was carefully controlled by a throttle valve positioned in front of the turbo pump, ensuring a consistent and controlled environment for the treatment. The parameters for the hydrogen plasma treatment were finely tuned to achieve a dual objective: the regeneration of the hydrogen termination (H-Termination) on the diamond surface while simultaneously safeguarding the Hafnium

oxide layer against any potential etching or surface deformation. Following this treatment, the substrate was allowed to cool down gradually within a hydrogen atmosphere. This controlled cooling process was designed to prevent any inadvertent oxidation of the surface, thus preserving the quality and functionality of both the diamond substrate and the newly formed HfO_2 layer.

1.11 Molybdenum metal deposition using E-Beam

Molybdenum metal deposition was carried out in an electron-gun evaporation vacuum chamber, with a base pressure of 6×10^{10} Torr monitored by a cold cathode gauge. The vacuum was maintained in a chamber with a turbomolecular pump, backed by an Adixen rotary oil pump, with final UHV pressure achieved via a CTI cryopump. The chamber utilizes water-cooled walls such that outgassing from the chamber surfaces due to thermal radiation generated by the tungsten electron gun filament and heated crucible is mitigated, achieving a high purity deposition with minimal incorporation of gaseous impurities. The metal evaporate source utilizes Molybdenum pellets of 99.999% purity, placed in a tungsten crucible within a 3kW electron beam evaporator from Thermionics. The electron gun voltage during the metal deposition was fixed at 6.41 kV, with a target deposition current of 70 mA. Throughout the deposition, the deposition rate was monitored with a Scion quartz crystal monitor (QCM) to ensure a stable evaporation rate.

The deposition procedure began with a preconditioning step of the metal crucible to remove adsorbates and initiate the power ramp, during which the beam current was held at 10 mA for 2 minutes. The beam current was then increased linearly at a rate of 10 mA/minute to 70 mA. Upon reaching 70 mA, the current was maintained for an

additional 3 minutes, during which a constant deposition rate of 0.035 Å/s was verified via the QCM, before opening the sample shutters to begin the deposition. The deposition extended over 3 minutes, for a total molybdenum thickness of 0.4 nm, after which both the crucible and sample shutters were closed. 0.4 nm of molybdenum metal thickness was chosen to allow for a complete oxidation of the metal layer after oxygen plasma in the subsequent processing step. Following the deposition, both the sample and crucible were allowed to cool in the chamber for a total of 10 minutes, after which the pressure reached 1.9×10^{-9} Torr.

1.12 Oxygen plasma treatment to oxidize Mo to MoO_3

After Mo deposition the substrates were again transferred to a remote plasma enhanced atomic layer deposition (PEALD) system to undergo the oxygen plasma process. The desired MoO_3 (+6) oxidation state was achieved through a controlled oxygen plasma treatment, applied for 5 minutes at ambient temperature with an oxygen flow rate of 30 sccm. The RF power was judiciously set to 30 W, carefully chosen to prevent high-intensity plasma from causing over-oxidation of the dielectric layers. The chamber was maintained at an oxygen pressure of 100 mTorr with the assistance of a throttle valve located near the turbo pump to ensure a stable and uniform plasma environment.

1.13 Photoemission Spectroscopy

The hole accumulation layer and the band bending of the diamond surface region was further corroborated using the binding energy of the core levels and Valence Band Minimum (VBM). The in situ XPS and UPS measurements were performed after each process step to measure the valence band offsets. This XPS/ UPS system has a base

pressure of 2×10^{-9} Torr. The XPS portion consists of monochromated Al K_α with a photon energy of 1486.7 ev and a narrow bandwidth of 0.2 eV. All core level spectra were recorded with a 0.05 eV step and peak positions were resolved with a 0.05 ev curve fitting.

For UPS, a high intensity UV source optimized for He I and He II radiation, at 21.2 Ev and 40.82 eV respectively were used. The UPS system utilized a helium discharge lamp and quartz-crystal monochromator in order to selectively illuminate the sample using He-IIα (40.81 eV) radiation and remove the spectral convolution contributions from other helium plasma excitations, primarily He-IIβ & He-IIγ in the high kinetic energy regions and He-Iα & He-Iβ in the low kinetic energy regions. The discharge pressure just outside the plasma region during the measurements was determined using a capacitance manometer as 2.20 $*10^{-1}$ Torr, with a discharge current and voltage of 100 mA and 1 kV, respectively. The discharge conditions within the helium plasma typically dictate the fractional photocurrent intensity ratio of Helium I to Helium II excitations, where a low plasma pressure increases the ratio of He-II to He-I excitations at the cost of the total available discharge species. These discharge conditions for fixed electrical parameters are optically visible within the plasma as a characteristically “peach” (He-I dominant) or “lilac” (He-II dominant) color. The He-IIα radiation incident on the sample after passing through the monochromator is maximized using a gold sample, which results in a “peach” plasma discharge condition for this experimental setup. Other typical (non-monochromated) UPS systems rely primarily on He-Iα excitations for Secondary Electron Cut Off (SECO) measurements related to the sample work function, and He-IIα excitations for measurements of the valence band occupation. Precise measurements of the valence band

occupation in a He-II dominant plasma are made difficult due to the contribution of the He-IIβ line (48.37 eV) ~8 eV higher than the primary excitation. This results in a relatively high intensity near and even above the Fermi level, which renders the determination of the valence band maximum difficult. Additionally, other systems would require an alteration of the plasma conditions in order to maximize the intensity of either He-I or He-II excitations, with lower pressures favoring He-II intensity maximization to Both the valence band occupation and secondary electron cutoff could each be precisely determined for the samples without altering the experimental conditions within the helium plasma discharge source. The stability of the plasma discharge conditions between the two measurements reduced the He-IIα photocurrent variation. The experimental setup solves these issues with the use of the crystalline quartz monochromator to eliminate nearly all intensity from the plasma other than the selected wavelength. The radiation generated via helium gas (UPS or the aluminum anode (XPS) is monochromated through either the XPS or UPS monochromator and impinges on the analyzed sample. The generated photoelectrons are collected and focused through a 0.8 mm analyzer slit via an electrostatic lens stack, after which the kinetic energy intensity distribution is analyzed via a hemispherical kinetic energy analyzer by sequentially selecting particular incident electron kinetic energies inside the analyzer and changing the kinetic energy to a fixed “pass energy” through the hemisphere of 10 eV for UPS, and 100 eV for XPS, resulting in an analyzer resolution of 30 meV for UPS and 0.3 eV for XPS.

1.14 Hall Measurements.

In this study, the Hall effect measurements were conducted using a Van der Pauw setup, where the four-point probes are strategically positioned at the corners of a square-shaped sample. This setup enables the determination of sheet resistance by inducing a current along one side of the sample while measuring the voltage across the opposite side. The resistance is calculated using Ohm's law, and, with the assumption of a uniform sample surface, the sheet resistance (Rs) is estimated by the formula:

$$\boldsymbol{R_s = \frac{\pi R}{ln2}} \qquad \textbf{\textit{Equation 0.1}}$$

Where R is the average resistance obtained from the four edges of the sample.

R can be further calculated as: $\boldsymbol{R = \frac{V}{I}}$ ***Equation 0.2***

V is the measured voltage, and I is the current flowing through the sample.

To further analyze the sheet carrier concentration (ns) and mobility (μ), a current is directed diagonally across the sample. An external magnetic field, perpendicular to the current, is applied, and the resultant Hall voltage (|VH|) is measured across the alternate diagonal. The Hall voltage is accurately determined by reversing the magnetic field and current directions and then averaging the outcomes.

These measurements were performed using an Ecopia HMS-3000 Hall Measurement System , equipped with a precise constant current source ranging from 1 nA to 100 mA. Samples were affixed on a spring clip board with four gold-plated tips, as illustrated in Figure 0.2, and positioned within a 0.55 T permanent magnet with a 26 mm pole gap, ensuring accurate measurement at room temperature. To ensure the validity of

the Van der Pauw method, ohmic contact integrity was confirmed via I-V measurements, providing a reliable basis for evaluating the electrical properties of diamond samples.

This methodical approach to Hall effect measurements not only yields essential parameters like sheet resistance, carrier density, and mobility but also offers insights into the intrinsic electrical characteristics of the diamond samples under investigation, contributing to a deeper understanding of their potential for electronic applications.

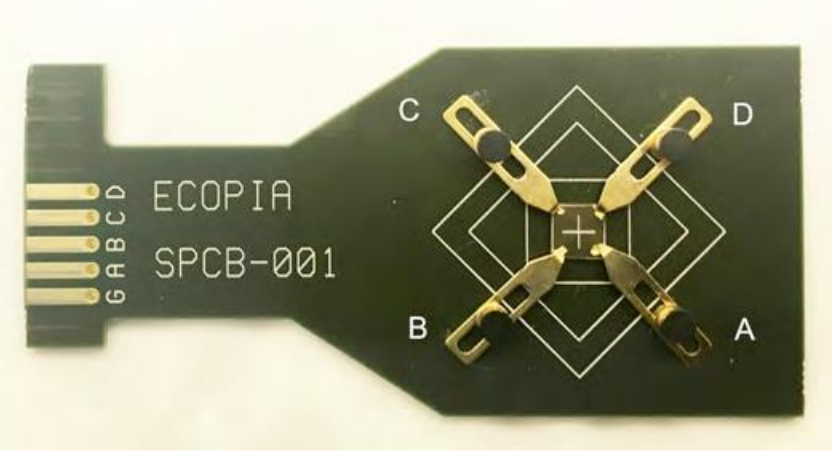

Figure 0.2 Photograph of a 5×5 mm2 diamond mounted on Ecopia HMS-3000clip board for sheet resistance and Hall effect measurement.

CHAPTER 3

RESULTS

2.1 Photoelectron spectroscopy (PES) characterization:

In the initial experiments, intrinsic diamond samples with MoO_3 as the acceptor layer were prepared with varying HfO_2 interfacial layers (0, 2 nm, 4 nm, 8 nm), deposited via thermal ALD. Typically, HfO_2 from thermal ALD exhibits significant leakage currents due to trap-assisted tunneling, impacting its dielectric properties.[48] [49] For C 1s, the peak at ~284.1 eV aligns with the sp^2-hybridized carbon typical of diamond's conductive state while shifts towards higher binding energies (~285 eV) suggest downward band bending (Figure 2.1), likely due to C-O bonds and trapped defects.

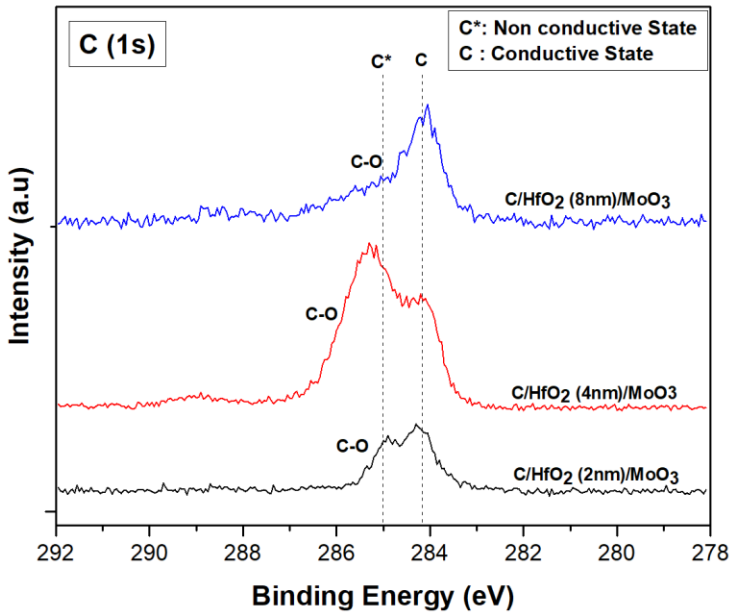

Figure 2.1 : XPS scan for C 1s core after HfO_2/ MoO_3 deposition for 2nm, 4nm and 8nm Hafnium oxide interfaces deposited by Thermal ALD.

As hafnium interfacial thickness increases the C 1s core levels shifted towards lower binding energy, that is the substrate became more conducive as interfacial layer thickness increased This could be due to reduced influence of interface defects and better charge impurity screening in thicker HfO_2 layers, thereby improving carrier mobility. The exact mechanisms underlying these observations are complex and may depend on various processing conditions and material properties, necessitating further detailed analysis to fully understand these trends.

In the second experiment series, Plasma Enhanced ALD was employed to deposit HfO_2 films on intrinsic single-crystalline diamond substrates. The substrates experienced charging during XPS measurements, which impeded analysis of the photoemission results. This contrasts with the non-charging behavior after Thermal ALD deposition, suggesting a link between the deposition method and substrate charging. During XPS, photoelectrons are ejected, leaving behind positive charges. The high-quality, low-defect HfO_2 layer produced by Plasma ALD lacks conductive defects, leading to charge accumulation and substrate charging during XPS. Conversely, the Thermal ALD HfO_2 layer, with a higher defect density, likely allows charge dissipation through defect-induced pathways, mitigating charging effects. These observations underscore the complex dynamics between deposition techniques, film quality, and substrate interaction affecting electronic properties.

In the third and fourth experiment series, substrates of highly boron-doped polycrystalline diamond (with a charge concentration of $10^{20}/\,\mathrm{cm}^2$) from E6 and medium boron-doped epitaxial layers on single-crystal diamond (SCD) substrates (with a

charge concentration of $10^{18}/\,cm^2$) from E6 were utilized. Both sets exhibited similar trends in Photoemission Spectroscopy measurements. On the hydrogen-terminated diamond surfaces, the C 1s core level was consistently observed at 284.1 eV, indicating effective surface passivation by hydrogen atoms.(Figure 2.2) This passivation plays a crucial role in reducing dangling bonds and surface states, thereby mitigating carrier trapping and recombination.

For optimal device performance, it is essential that these H-terminated surfaces remain free from adsorbates that could adversely affect their electrical properties. The absence of an O 1s peak in the spectra corroborates the lack of C-O bonds and adsorbates, affirming the surface purity. (Figure 2.3) Additionally, Ultraviolet Photoelectron Spectroscopy (UPS) using He II radiation revealed the Valence Band Maximum (VBM) of the H-terminated diamond at 0.3 eV (Figure 2.6), further confirming the p-type nature of the surface. This comprehensive characterization underscores the substrates' suitability for high-performance electronic applications.

Figure 2.2, Figure 2.3, Figure 2.4 present the core-level spectra of C 1s, O 1s, and Hf 4f, respectively, captured at various stages of the fabrication process. The sequential processes are delineated as follows: (i) Hydrogen termination, (ii) Hafnium oxide Atomic Layer Deposition (ALD), (iii) Hydrogen plasma treatment, and (iv) Molybdenum trioxide (MoO_3) deposition. Additionally, Figure 2.5 specifically illustrates the Mo 3d core levels post the electron-beam (E-Beam) deposition of Mo and the subsequent oxidation process converting Mo to MoO_3

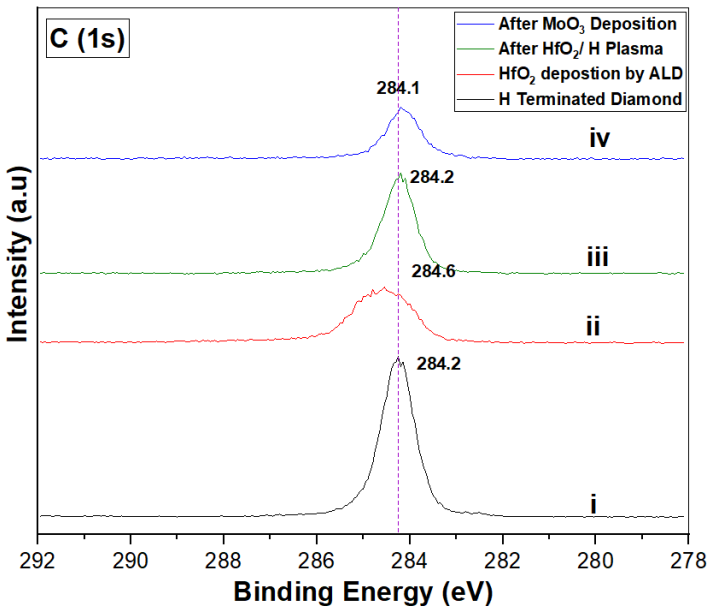

Figure 2.2 : XPS scan for C 1s core levels after each process

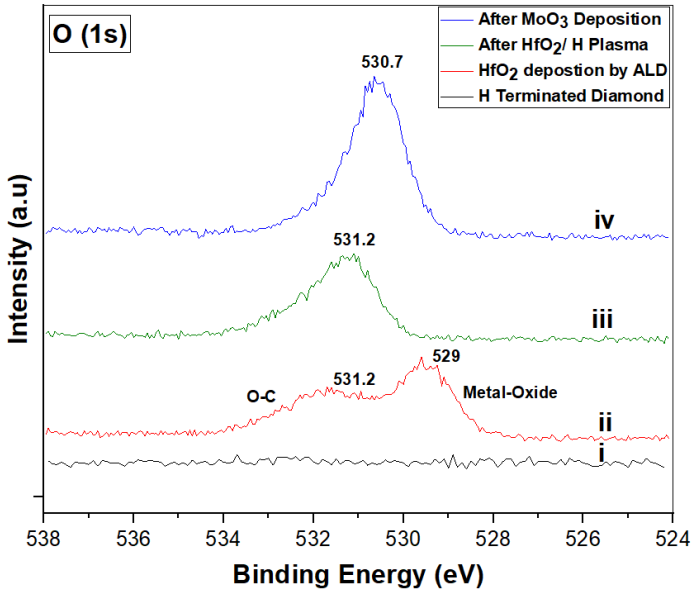

Figure 2.3: XPS scan for O 1s core levels after each process

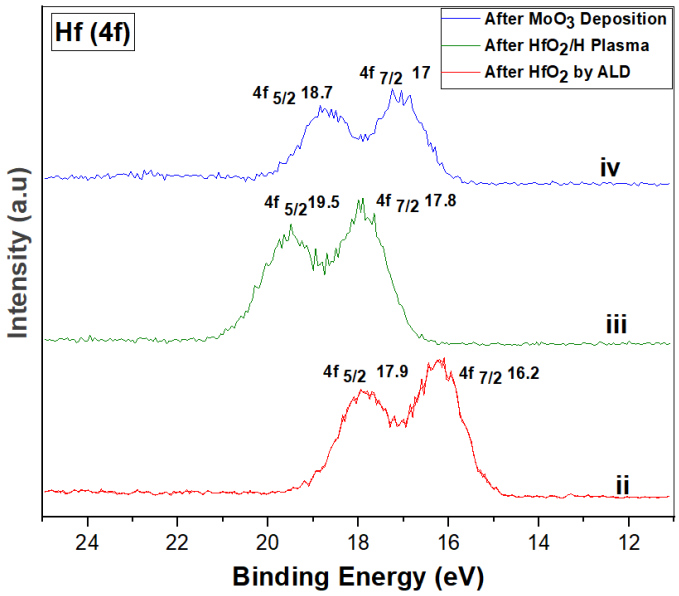

Figure 2.4: XPS scan for Hf 4f core levels after each process

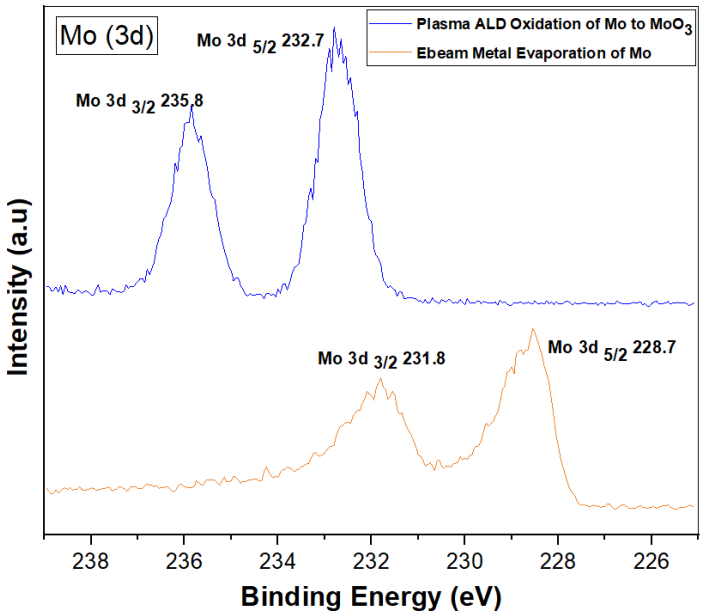

Figure 2.5: XPS scan for Mo 3d core levels

After deposition of ~2nm HfO_2, Hf 4f peaks were observed at 17.9 and 16.2ev respectively (Figure 2.4) , the peaks shifted by around 2 eV from original anticipated Hf

metallic peaks, indicating that a thin HfO_2 film was fabricated on the diamond. However, the C 1s peak shifted to a higher binding energy of 284.6 eV (Figure 2.2) indicating a transition from upward band bending to downward band bending and a reduction of surface accumulation density. The FWHM of C 1s peak increased from 0.9 eV to 1.4 eV indicating the peak broadening and incorporation of some defects. In Figure 2.3, broadening of the O 1s peak was observed. The higher binding energy of the O 1s core level indicates the formation of C-O bonds, and the O 1s peak at 529 eV indicates the oxygen rich state of Hafnium oxide. After Hydrogen plasma, (Figure 2.2) the C 1s binding energy was restored back to the same level as the conductive diamond surface, while the FWHM was C 1s also reducing to 0.8 ev. In Figure 2.4, Hf 4f peaks shifted by 1.6 ev indicating that the hydrogen plasma not only restored the hole accumulation layer in diamond, but also healed the defects in the dielectric resulting in negatively charged layer at the interface. The negatively charged interfacial layer, which is directly adjacent to the diamond hole accumulation layer, would increase the Coulomb scattering of the holes, limiting the hole mobility. After MoO_3 deposition, the Hf core levels shifted back to lower binding energy by 0.8 ev (Figure 2.4) , indicating a reduced density of charges near the diamond surface. This can be explained by the formation of a dipole near the MoO_3/ HfO_2 interface transferring negative charges from Diamond/ Hafnium interface to the Hafnium Oxide/ MoO_3 interface. This resulted in reduced Coulomb scattering. The C 1s core level position shifted by 0.1 ev (Figure 2.2) towards lower binding after MoO_3 deposition energy relative to H-Terminated conductive diamond confirming the increased conductivity and upward band bending.

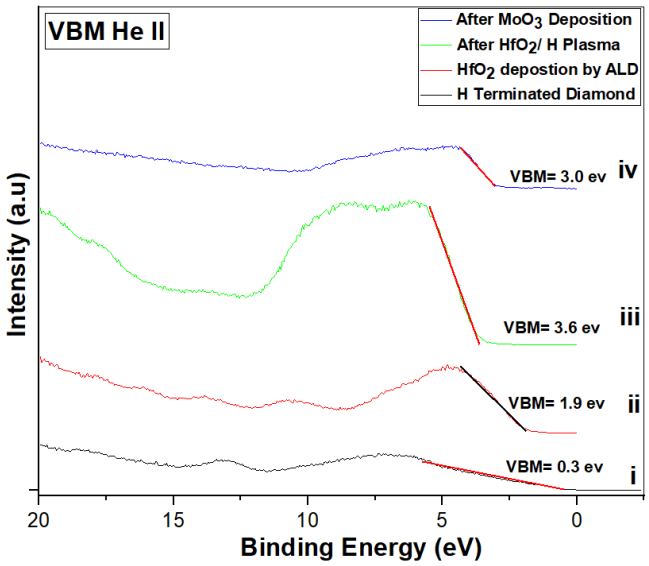

Figure 2.6 : UPS Scans Post-Process Steps for VBM Determination

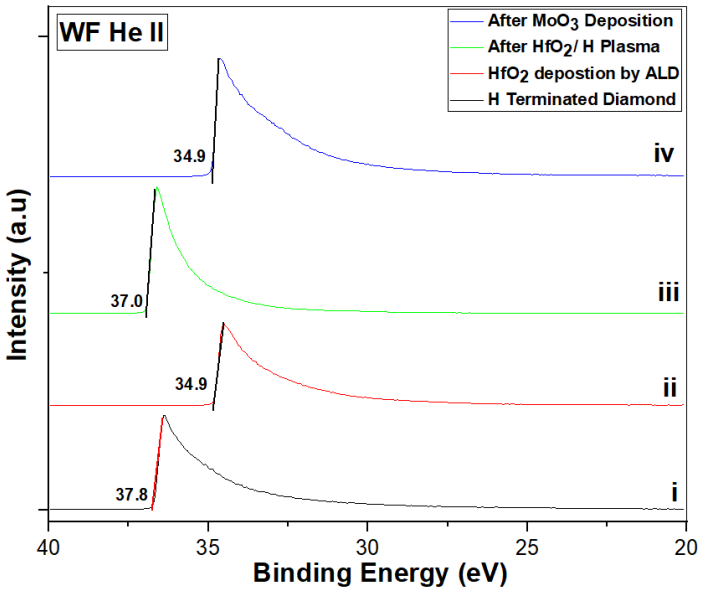

Figure 2.7 : UPS Scans Post-Process Steps for WF Determination

The Valence Band Maximum (VBM) is determined by extrapolating the low binding energy cutoff to intersect with a linear fit of the background noise above the Fermi level, as demonstrated in Figure 2.6. This intersection point is interpreted as the VBM. For

hydrogen-terminated diamond, which exhibits a Negative Electron Affinity (NEA), the vacuum level resides below the Conduction Band Minimum (CBM). The electron affinity (χ) is calculated as the difference between the CBM and the vacuum energy (Evac).

The Work Function (Φ) is deduced by subtracting the binding energy associated with the He II α line (40.8 eV) from the energy at the base of the linear fit of the high binding energy cutoff, as evident from Figure 2.7. Using this method, the VBM and Work Function for H Terminated Diamond were found to be 0.3 eV and 4 eV, respectively. The electron affinity can be further calculated using the formula

$$\chi = \Phi + (E_F - E_{vbm}) - Eg \quad [50] \qquad \textit{Equation 2.1}$$

For our measurements:

χ = 4 ev +0.3 ev– 5.4 ev = -1.1 ev

This NEA value of H-Terminated Diamond, as determined by UPS, aligns with findings reported by Takeuchi et al. in 2005 [27], confirming the consistency of the methodology.

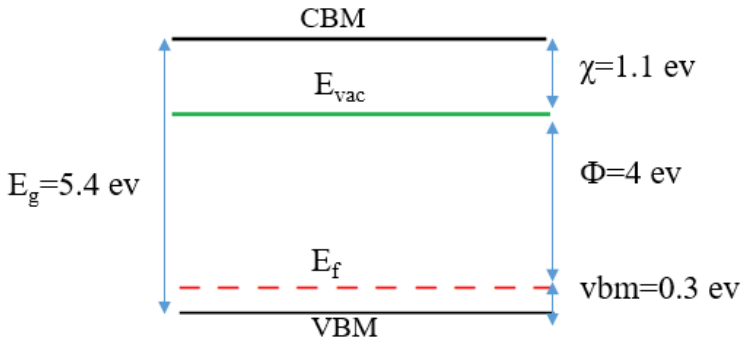

Figure 2.8 : Band Schematic of Hydrogen Terminated Diamond

After PE-ALD of Hafnium , the work function of Hafnium oxide was found to be 5.9 ev (Figure 2.7) which is similar to MoO_3 work function. The large work function of HfO_2 can be attributed to oxygen vacancies and defects. The hydrogen plasma process heals the defects, and the work function is reduced to 4.8 eV. The band gaps for these materials are as follows: 5.6 eV for HfO_2 [48,44], and 2.8 eV for MoO_3 [51,52]. The calculated electron affinities are 2.5 eV and 5.9 eV for HfO_2 and MoO_3 respectively using equation 3.1

Post Hafnium oxide deposition, the VBM for HfO_2 was observed at 1.9 eV, highlighting HfO_2's passivation properties. Following H- Plasma treatment, the VBM shifted to 3.6 eV, indicating the plasma's role in diminishing HfO_2 defects and enhancing its passivation effect. Finally, after MoO_3 deposition, the Valence Band Minimum was observed at 3 eV, suggesting MoO_3's CBM is positioned at or below the VBM of the H-terminated diamond.

2.2 Hall electrical characterization

The electrical properties of the semiconductor interfaces were quantitatively assessed using a Hall measurement system. The key parameters investigated included sheet concentration (n_s), hole mobility (μ), and sheet resistance (R_s). These properties are interrelated and crucial in evaluating the performance of the semiconductor interfaces.

The sheet concentration $\boldsymbol{n_s}$ was determined using the Hall Effect ***Equation 2.2:***[53]

$\boldsymbol{n_s = \frac{1}{e.R_H}}$ where $\boldsymbol{R_H}$ is the Hall coefficient and e is the elementary charge.

Hole mobility (μ), was calculated using Brooks- Herring and Conwell- Weisskopf approximations as described by ***Equation 2.3*** [54]

$$\mu = \frac{8\sqrt{2}}{q^3}\,\frac{k^{\frac{3}{2}}}{\pi}\,\frac{\varepsilon_r{}^2 \mathrm{T}^{\frac{3}{2}}}{(m^*)^{\frac{1}{2}}}$$

where k is the Boltzmann constant, q is the electron charge, ε_r is the relative permittivity, m^* is the effective mass, and f is the screening factor.

The Coulomb scattering mechanism results in a carrier mobility that is inversely proportional to the density of charged scattering centers. Finally, sheet resistance (Rs) was measured directly and is defined by Equation 2.4:

$Rs = \frac{1}{\mu q\,(n_s\,t)}$; t is the thickness of the material, and $(n_s\,t)$ is the sheet concentration.[55]

Table 4.1 summarizes the change of sheet concentration, hole mobility and sheet resistance of H-Terminated Diamond with MoO_3 as acceptor layer and HfO_2 as an interface layer. For the sample without HfO_2, the surface conductivity of diamond was achieved with MoO_3 as acceptor layer, which was reported by Yang et al 2022.[35] Yang et al noted that after MoO_3 deposition and oxidation, the sheet resistance increased to 6.9 kΩ/ sq and remained under 10 kΩ/ sq but the hole mobility decreased from 18.4 cm^2/ V-s to 8.9 cm^2/ V-s. For the samples with 2nm and 4 nm HfO_2 interfacial layer deposited by Thermal ALD the sheet resistance increased by an order of magnitude and the hole mobility reduced as well. For the samples with 8 nm HfO_2 interfacial layer deposited by Thermal ALD, the sheet resistance increased slightly, and hole mobility remained similar. The hole mobility doubled for the samples with 2 nm HfO_2 interfacial layer deposited by PEALD. The change in sheet resistance, hole concentration and hole mobility for the different structures with processes are plotted in Fig 4.10, and the hole concentration, mobility of different

structures are compared in Fig 4.11

Table 2.1 Hall measurement sheet resistance, carrier concentration and carrier mobility of diamond surfaces using MoO_3 as acceptor layer with 2, 4 and 8 nm HfO_2 interfacial layers.

Sample	Process	Sheet resistance (kΩ)	Carrier Concentration/ cm^2	Carrier Mobility cm^2/ V-s
0 nm HfO_2 Interfacial layer	H-Terminated Surface	1.8	1.9×10^{14}	18.4
	After MoO_3 dep.	6.9	1×10^{14}	8.9
2 nm thermal ALD grown HfO_2 Interfacial layer	H-Terminated Surface	356	6.5×10^{12}	2.7
	After HfO_2/ MoO_3 deposition	3470	9.0×10^{11}	2
4 nm thermal ALD grown HfO_2 Interfacial layer	H-Terminated Surface	146	8.4×10^{12}	5.1
	After HfO_2/ MoO_3 deposition	871	1.5×10^{12}	4.7
8 nm thermal ALD grown HfO_2 Interfacial layer	H-Terminated Surface	20	1×10^{13}	31
	After HfO_2/ MoO_3 deposition	31	6.3×10^{12}	32
2 nm Plasma ALD grown HfO_2 Interfacial layer	H-Terminated Surface	110	7.1E11	80
	After HfO_2/ MoO_3 position	710	5.5E10	160

CHAPTER 4

DISCUSSION

3.1 Band alignment of H-Terminated diamond/ HfO_2 / MoO_3

The VBO (ΔE_v) of the interface can be deduced using the method presented by Walldrop, Kraut and Grant shown in the equation:[56,57]

$$(\Delta E_v) = (E_{CL}\text{-}Ev)_C - (E_{CL}\text{-}Ev)_{HfO2} - \Delta E_{CL}$$

Here E_{CL} signifies the binding energy of the XPS core level, E_v represents the valence band maximum (VBM); ΔE_{CL} is defined as the binding energy difference between the core level of diamond and HfO_2 measured at the interface ($E_{CL}^{C1s} - E_{CL}^{Hf\,4f}$); (E_{CL}-Ev) is the energy difference between respective binding energy of core levels and their VBM. The measured value of $(E_{CL}\text{-}Ev)_{HfO2}$ was 264.7 eV and $(E_{CL}\text{-}Ev)_C$ was 283.9 eV. The HfO_2 layer's VBM was noted to be 3.6 eV below the Fermi level, and the H-terminated diamond's VBM was 0.3 eV below the Fermi level. Utilizing this data, the VBO between HfO_2 and diamond was calculated as 3.3 eV. Additional, band bending of 1.6 eV measured using XPS can be attributed to defect concentrations or interstitial oxygen atoms in the HfO_2 layer, introduced during oxygen plasma processing.

For the diamond and MoO_3 interface, the VBO was calculated similarly:

$$(\Delta E_v) = (E_{CL}\text{-}Ev)_C - (E_{CL}\text{-}Ev)_{MoO3} - \Delta E_{CL}$$

The $(E_{CL}\text{-}Ev)_{MoO3}$ value was determined to be 229.7 eV and ΔE_{CL} was calculated as 51.4 eV. The VBO between MoO_3 and diamond was determined to be 2.8 eV.

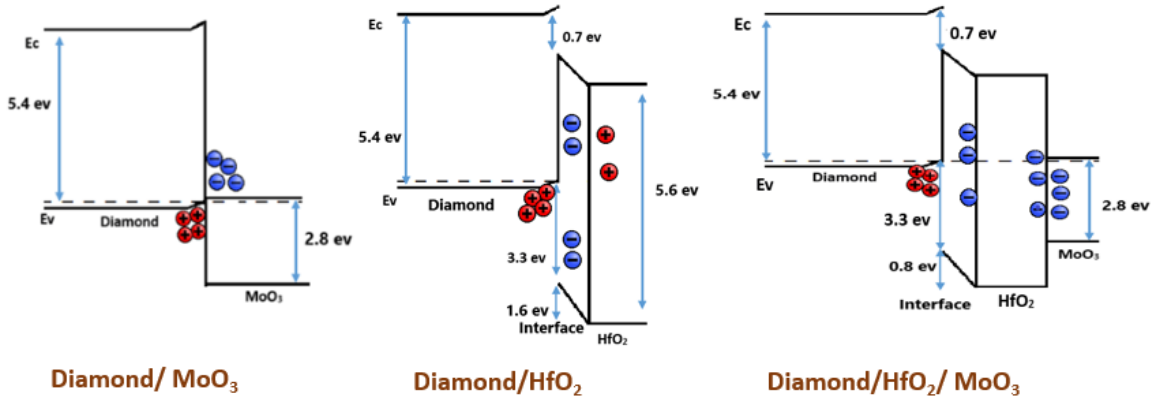

Figure 3.1 The Band Diagram of diamond / MoO_3 and diamond / HfO_2 / MoO_3 before and after MoO_3 deposition

The band diagrams of diamond/ HfO_2 and diamond / HfO_2 / MoO_3 are shown in Fig. 4.1. The charge at the H-terminated diamond and HfO_2 is represented by a decrease of the interface band shift. After HfO_2 deposition, the VBM of diamond is clearly separated from CBM of HfO_2 thus showing the passivation property of HfO_2 to separate the charges. After MoO_3 is deposited on HfO_2, the Hf 4f core level is shifted towards lower binding energy. The distribution of negative charges has changed and a fraction of negative charges originally close to diamond transferred into the MoO_3. This observation is consistent with the goal of displacing the charge from the interface.

3.2 Tunneling and understanding the physics behind the charge transfer.

In the semiconductor structure comprised of H-Terminated Diamond, HfO_2, and MoO_3, charge transfer and tunneling are profoundly influenced by the unique electronic properties

of these materials. The H-Terminated Diamond, characterized by a Negative Electron Affinity (NEA) of 1.1 eV and a bandgap of 5.4 eV, establishes a foundational electronic landscape for this interface. The HfO_2 and MoO_3 layers, with electron affinities of 2.5 eV and 5.9 eV, and bandgaps of 5.6 eV [48, 46], and 2.8 eV[51], [52] respectively, further modulate this landscape. Given the work functions—4 eV for diamond, 4.8 eV for HfO_2, and 5.9 eV for MoO_3—the formation of dipoles at the interfaces introduces distinct electric fields, influencing band alignment and charge dynamics.

The dipole at the HfO_2/diamond interface, pointing towards the diamond, facilitates hole accumulation in the H-Terminated Diamond. This arrangement, along with the diamond's NEA, creates a favorable condition for tunneling holes through the HfO_2 layer, despite its wide bandgap. The electric field resulting from this dipole orientation aids in maintaining the holes at the diamond surface, while also potentially reducing scattering effects caused by interface charges or defects. On the other hand, at the HfO_2/MoO_3 interface, the dipole's orientation, from MoO_3 towards HfO_2, aligns with MoO_3's higher work function. This creates a potential barrier that electrons in the MoO_3 must overcome to tunnel through the HfO_2 layer. The combination of the MoO_3 bandgap, electron affinity, and the dipole-induced electric field shapes the electron transfer from MoO_3 to the diamond, mediated by the HfO_2 layer. The band alignment and dipole effects at this interface are critical in preventing direct recombination of electrons and holes, thus enhancing the charge separation essential for efficient device operation.

The charge transfer in this multilayer semiconductor structure is a delicate interplay of material-specific properties, including work functions, bandgaps, and electron affinities,

along with the resultant electric fields and dipoles at the interfaces. The understanding and manipulation of these phenomena are pivotal in achieving desired electronic characteristics and enhancing the performance of devices utilizing this unique material assembly.

3.3 Understanding Electrical Measurements

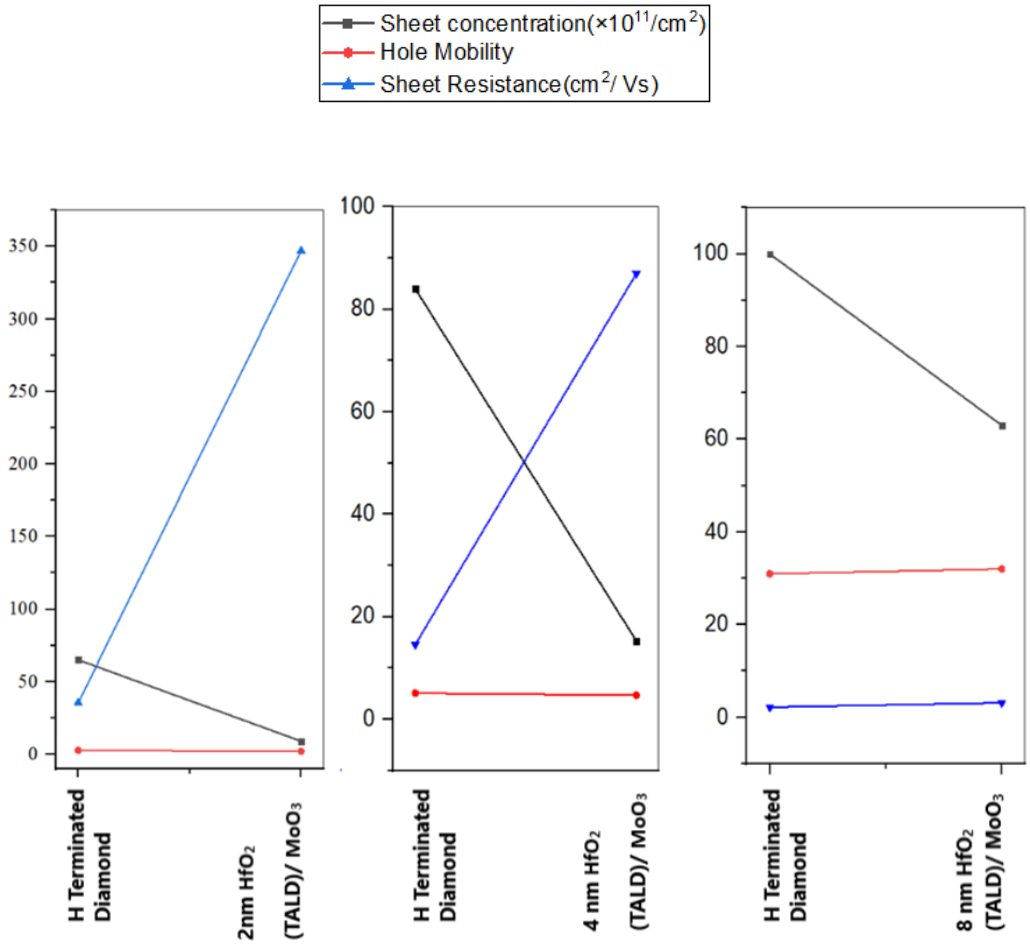

Figure 3.2 Change in sheet resistance, hole concentration and hole mobility with processes for diamond/ MoO3 with 2,4, 8 nm HfO2 interfacial layers deposited by TALD

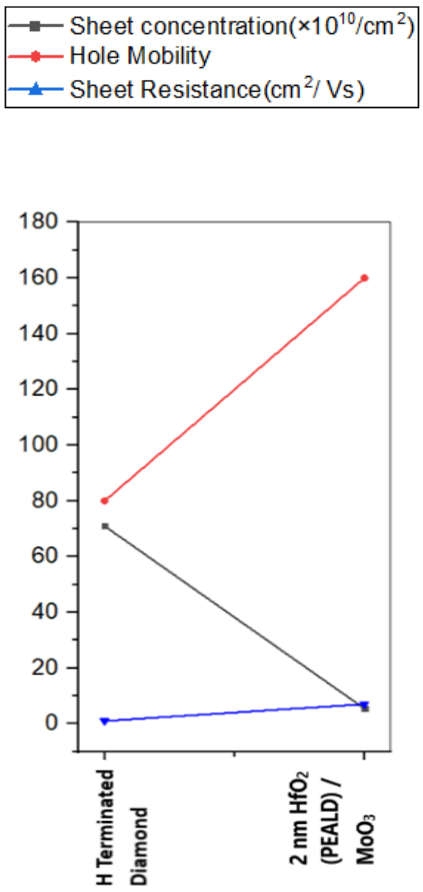

Diamond / 2 nm HfO_2 (PEALD) / MoO_3

Figure 3.3 Change in sheet resistance, hole concentration and hole mobility with processes for diamond/ MoO3 with 2 nm HfO2 interfacial layers deposited by PEALD

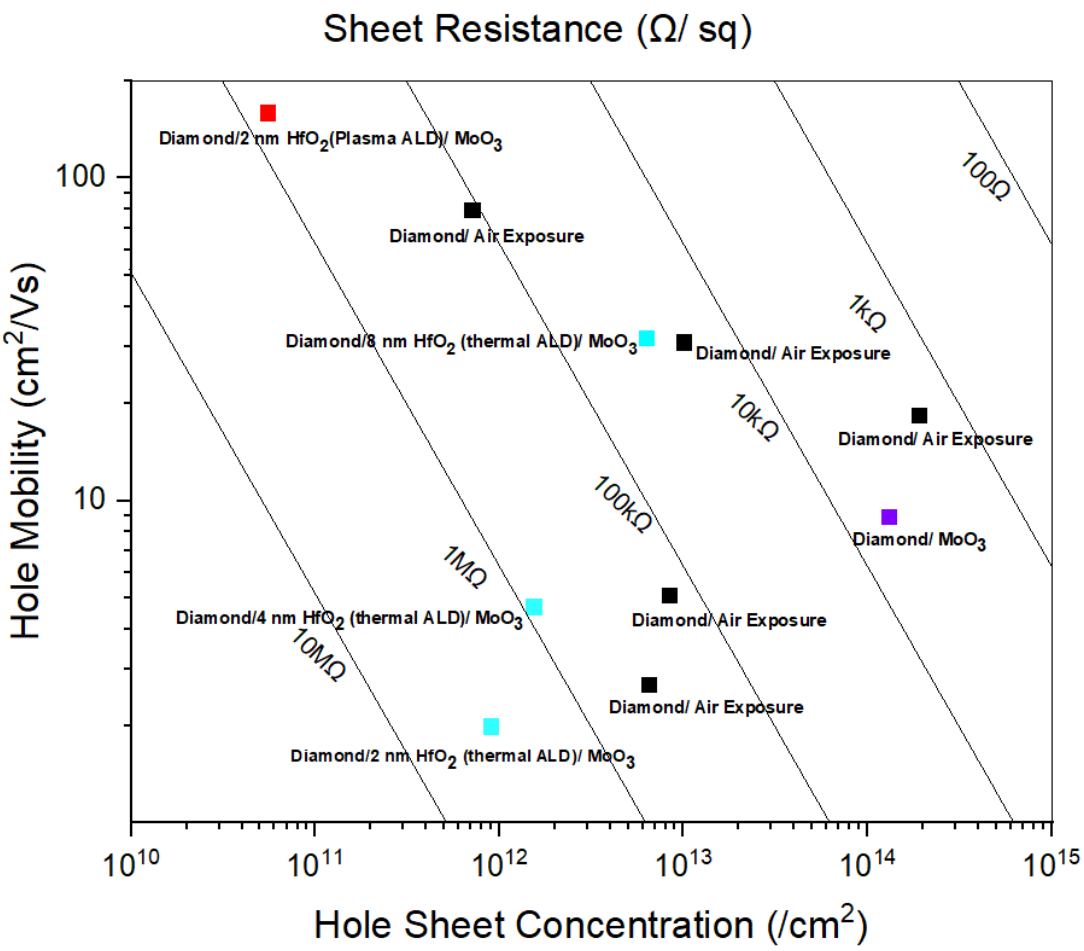

Figure 3.4 Hole concentration and mobility comparison of different structures

In Figure 3.2 and Figure 3.3, The contrast in the electronic properties of the interfaces with HfO_2 layers of the same thickness (2 nm) deposited by Thermal ALD (TALD) and Plasma Enhanced ALD (PEALD) can be attributed to the differences in the deposition processes and the resulting film characteristics. These differences, along with the varying thicknesses in the TALD process, can significantly impact carrier mobility.

In TALD, the growth of the HfO_2 layer results in films with higher defect densities, especially at lower thicknesses like 2 nm.[48,49, 58], These defects function as scattering centers or traps, adversely affecting carrier mobility and increasing sheet resistance.

As the thickness increases (4 nm and 8 nm), the density of interface states and traps that directly influence the diamond surface decreases. [59] This results in improved screening and a reduction in the scattering or trapping of carriers, leading to the observed increase in mobility and stabilization of sheet resistance relatively.

PEALD, with its use of plasma, tends to produce denser and more uniform films, even at lower thicknesses like 2 nm.[45], [60] The enhanced quality of the 2 nm HfO_2 layer deposited by PEALD provided better dielectric screening and reduced the impact of surface states or traps. This results in a significant improvement in carrier mobility, as observed in Figure 3.3 and Figure 3.4

Additionally, the plasma process alters interface chemistry in a way that is more conducive to carrier transport compared to TALD, further enhancing mobility. The increase in sheet resistance can be attributed to the large dielectric constant (25) of Hafnium oxide[47], [61].

CHAPTER 5

CONCLUSION:

In this study, a surface conductive layer was established on hydrogen-terminated diamond utilizing Hafnium Oxide (HfO_2) as a modulation doping layer and Molybdenum Trioxide (MoO_3) as the surface acceptor layer. Valence Band Offsets (VBO) were identified as 3.3 eV for the HfO_2/H-Terminated Diamond interface and 2.8 eV for MoO_3/H-Terminated Diamond, providing a conducive environment for charge transfer due to the advantageous band alignment.

Diamond's sheet resistance, hole concentration, and mobility for configurations involving MoO_3/H-diamond with HfO_2 interfacial layers of 2, 4, and 8 nm thicknesses applied through Thermal Atomic Layer Deposition (TALD), alongside a 2 nm thickness deposited by Plasma Enhanced Atomic Layer Deposition (PEALD) were characterized. This methodical incorporation of dual oxides enabled the modulation of hole mobility and concentration by adjusting the thickness of the HfO_2 interfacial layer. Importantly, the insertion of an interfacial layer via PEALD markedly improved the mobility within the hole accumulation layer which we attribute to a reduction of interface scattering, underscoring the superior interfacial layer quality achieved through PEALD compared to TALD. However, the 8 nm layer deposited by TALD demonstrated notable performance.

The findings indicated that overall sheet resistance across varying HfO_2 interlayer thicknesses decreased with an increase in layer thickness yet remained higher compared to the MoO_3/Diamond interface lacking an interfacial layer. This underscores that charges at the HfO_2/H-diamond interface continue to impede mobility.

Enhancements in the HfO_2/H-diamond interface, informed by comprehensive structural and chemical analyses along with Hall measurements, are anticipated to significantly influence interface mobility. Furthermore, the promising results from the recent application of a 2 nm HfO_2 layer via PEALD highlight the potential for further exploration of the same dielectric material with 4 nm and 8 nm interfaces. This in-depth examination aims to advance the understanding of how dielectric materials can optimize the functionality of H-diamond electronic devices.

REFERENCES

1. Wort, C. J. H. & Balmer, R. S. Diamond as an electronic material. *Mater. Today* **11**, 22–28 (2008).

2. Kasu, M., Ueda, K., Yamauchi, Y., Tallaire, A. & Makimoto, T. Diamond-based RF power transistors: Fundamentals and applications. *Diam. Relat. Mater.* **16**, 1010–1015 (2007).

3. Kohn, E. & Denisenko, A. Concepts for diamond electronics. *Thin Solid Films* **515**, 4333–4339 (2007).

4. Isberg, J. *et al.* High carrier mobility in single-crystal plasma-deposited diamond. *Science (80-.).* **297**, 1670–1672 (2002).

5. Gabrysch, M., Majdi, S., Twitchen, D. J. & Isberg, J. Electron and hole drift velocity in chemical vapor deposition diamond. *J. Appl. Phys.* **109**, 63719 (2011).

6. Hatch, K. A. *et al.* External charge compensation in etched gallium nitride measured by x-ray photoelectron spectroscopy. *J. Appl. Phys.* **131**, 185301 (2022).

7. Brown, F. G., Gilland, J., Hassig, R. & Boese, R. W. Pioneer-Venus Large Probe Infrared Radiometer (LIR) Optical System. in *21st Annual Technical Symposium* (ed. Spiro, I. J.) 132–138 (1977). doi:10.1117/12.955851.

8. Umezawa, H. Recent advances in diamond power semiconductor devices. *Mater. Sci. Semicond. Process.* **78**, 147–156 (2018).

9. Baliga, B. J. Power Semiconductor Device Figure of Merit for High-Frequency Applications. **10**, 455–457 (1989).

10. Huang, A. Q. & Member, S. New Unipolar Switching Power Device Figures of Merit. **25**, 298–301 (2004).

11. Coltrin, M. E. & Kaplar, R. J. Transport and breakdown analysis for improved figure-of-merit for AlGaN power devices. **055706**, (2017).

12. Tsao, J. Y. *et al.* Ultrawide-Bandgap Semiconductors: Research Opportunities and Challenges. *Adv. Electron. Mater.* **4**, (2018).

13. Inushima, T., Matsushita, T., Ohya, S. & Shiomi, H. Hopping conduction via the excited states of boron in p-type diamond. *Diam. Relat. Mater.* **9**, 1066–1070 (2000).

14. Tsukioka, K. & Okushi, H. Hall mobility and scattering mechanism of holes in boron-doped homoepitaxial chemical vapor deposition diamond thin films. *Japanese J. Appl. Physics, Part 1 Regul. Pap. Short Notes Rev. Pap.* **45**, 8571–8577 (2006).

15. Isberg, J., Lindblom, A., Tajani, A. & Twitchen, D. Temperature dependence of hole drift mobility in high-purity single-crystal CVD diamond. *Phys. Status Solidi Appl. Mater. Sci.* **202**, 2194–2198 (2005).

16. Pernot, J. *et al.* Hall hole mobility in boron-doped homoepitaxial diamond. *Phys. Rev. B - Condens. Matter Mater. Phys.* **81**, 1–7 (2010).

17. Peterson, R. *et al.* Analysis of mobility-limiting mechanisms of the two-dimensional hole gas on hydrogen-terminated diamond. *Phys. Rev. B* **102**, 1–10 (2020).

18. Kalish, R. Ion-implantation in diamond and diamond films: Doping, damage effects and their applications. *Appl. Surf. Sci.* **117**–**118**, 558–569 (1997).

19. Jiménez-Riobóo, R. J. *et al.* Boron-doped diamond by 9 MeV microbeam implantation: Damage and recovery. *Carbon N. Y.* **208**, 421–431 (2023).

20. Landstrass, M. I. & Ravi, K. V. Resistivity of chemical vapor deposited diamond films. *Appl. Phys. Lett.* **55**, 975–977 (1989).

21. Mak, T. *et al.* Hydrogenating effect of single-crystal diamond surface. *Jpn. J. Appl. Phys.* **31**, L1446–L1449 (1992).

22. Hayashi, K. *et al.* Investigation of the effect of hydrogen on electrical and optical properties in chemical vapor deposited on homoepitaxial diamond films. *J. Appl. Phys.* **81**, 744–753 (1997).

23. Maier, F., Riedel, M., Mantel, B., Ristein, J. & Ley, L. Origin of surface conductivity in diamond. *Phys. Rev. Lett.* **85**, 3472–3475 (2000).

24. R.S. Gi, T. Mizumasa, Y. Akiba, Y. Hirose, T. Kurosu, M. I. No Title. *Jpn. J. Appl. Phys.* **34**, (1995).

25. Hirama, K. *et al.* Spontaneous polarization model for surface orientation dependence of diamond hole accumulation layer and its transistor performance. *Appl. Phys. Lett.* **92**, (2008).

26. Takeuchi, D., Ri, S. G., Kato, H., Nebel, C. E. & Yamasaki, S. Negative electron affinity on hydrogen terminated diamond. *Phys. Status Solidi Appl. Mater. Sci.* **202**, 2098–2103 (2005).

27. Takeuchi, D. *et al.* Direct observation of negative electron affinity in hydrogen-terminated diamond surfaces. *Appl. Phys. Lett.* **86**, 1–3 (2005).

28. Kawarada, H., Aoki, M. & Ito, M. Enhancement mode metal - semiconductor field effect transistors using homoepitaxial diamonds □. **1565**, 1563–1565 (1994).

29. Crawford, K. G., Maini, I., Macdonald, D. A. & Moran, D. A. J. Surface transfer doping of diamond: A review. *Prog. Surf. Sci.* **96**, 100613 (2021).

30. Moran, D. A. J., Russell, S. A. O., Cao, L., Qi, D. & Tallaire, A. Surface transfer doping of diamond by MoO 3 : A combined spectroscopic and Hall measurement study □. (2013) doi:10.1063/1.4832455.

31. Tordjman, M., Saguy, C., Bolker, A. & Kalish, R. Superior Surface Transfer Doping of Diamond with MoO 3. 1–6 (2014) doi:10.1002/admi.201300155.

32. Verona, C., Ciccognani, W., Colangeli, S., Limiti, E. & Marinelli, M. Comparative investigation of surface transfer doping of hydrogen terminated diamond by high electron affinity insulators. (2016) doi:10.1063/1.4955469.

33. Wang, X. *et al.* Reexamination of band offset transitivity employing oxide heterojunctions. *Appl. Phys. Lett.* **102**, 31605 (2013).

34. Hasegawa, K. Characterization of diamond metal-insulator-semiconductor field-effect transistors with aluminum oxide gate insulator □. (2006) doi:10.1063/1.2186072.

35. Yang, Y., Koeck, F. A., Wang, X. & Nemanich, R. J. Surface transfer doping of MoO3on hydrogen terminated diamond with an Al2O3interfacial layer. *Appl. Phys. Lett.* **120**, (2022).

36. Wang, W. *et al.* Diamond Based Field-Effect Transistors of Zr Gate with SiN ? Dielectric Layers. **2015**, 1–6 (2015).

37. Liu, J. W., Oosato, H., Liao, M. Y. & Koide, Y. Enhancement-mode hydrogenated diamond metal-oxide-semiconductor field-effect transistors with Y2O3 oxide insulator grown by electron beam evaporator. 2–7 (2017) doi:10.1063/1.4983091.

38. Saito, T. *et al.* Fabrication of Metal – Oxide – Diamond Field-Effect Transistors with Submicron-Sized Gate Length on Boron-Doped (111) H-Terminated Surfaces Using Electron Beam Evaporated SiO 2 and Al 2 O 3. **40**, 247–252 (2011).

39. Liu, J. W. *et al.* Electrical characteristics of hydrogen-terminated diamond metal-oxide-semiconductor with atomic layer deposited HfO2 as gate dielectric. *Appl. Phys. Lett.* **102**, 2–6 (2013).

40. Wang, W. *et al.* An Enhancement-Mode Hydrogen-Terminated Diamond Field-Effect Transistor With Lanthanum Hexaboride Gate Material. *IEEE Electron Device Lett.* **41**, 585–588 (2020).

41. Ren, Z., Zhang, J., Zhang, J. & Zhang, C. Diamond Field Effect Transistors With MoO 3 Gate Dielectric. *IEEE Electron Device Lett.* **38**, 786–789 (2017).

42. Yang, Y. Interface Electronic State Characterization of Dielectrics on Diamond and C-BN. (Arizona State University, 2018).

43. Ueda, K. *et al.* Diamond FET Using High-Quality Polycrystalline. **27**, 570–572 (2006).

44. Kim, J. *et al.* Characteristics of HfO 2 thin films grown by plasma atomic layer deposition. *Appl. Phys. Lett.* **87**, 10–12 (2005).

45. Zhang, X. Y. *et al.* Crystallinity Effect on Electrical Properties of PEALD–HfO2 Thin Films Prepared by Different Substrate Temperatures. *Nanomaterials* **12**, (2022).

46. Kim, K. M., Jang, J. S., Yoon, S. G., Yun, J. Y. & Chung, N. K. Structural, optical and electrical properties of HfO2 thin films deposited at low-temperature using plasma-enhanced atomic layer deposition. *Materials (Basel).* **13**, (2020).

47. Lin, Y. S., Puthenkovilakam, R. & Chang, J. P. Dielectric property and thermal stability of HfO2 on silicon. *Appl. Phys. Lett.* **81**, 2041–2043 (2002).

48. Martínez-Puente, M. A. *et al.* ALD and PEALD deposition of HfO2 and its effects on the nature of oxygen vacancies. *Mater. Sci. Eng. B* **285**, 115964 (2022).

49. Ahadi, K. & Cadien, K. Ultra low density of interfacial traps with mixed thermal and plasma enhanced ALD of high-κ gate dielectrics. *RSC Adv.* **6**, 16301–16307 (2016).

50. James, M. C. *et al.* Experimental Studies of Electron Affinity and Work Function

from Aluminium on Oxidized Diamond (100) and (111) Surfaces. *Phys. Status Solidi Basic Res.* **258**, 1–13 (2021).

51. Sivakumar, R., Gopalakrishnan, R., Jayachandran, M. & Sanjeeviraja, C. Characterization on electron beam evaporated α-MoO3 thin films by the influence of substrate temperature. *Curr. Appl. Phys.* **7**, 51–59 (2007).

52. Bhatia, S., Khanna, A., Jain, R. K. & Hirdesh. Structure-property correlations in molybdenum trioxide thin films and nanoparticles. *Mater. Res. Express* **6**, (2019).

53. Østerberg, F. W. *et al.* Hall effect measurement for precise sheet resistance and thickness evaluation of Ruthenium thin films using non-equidistant four-point probes. *AIP Adv.* **8**, (2018).

54. Somogyi, K. Classical approximations for ionised impurity scattering applied to diamond monocrystals. *Diam. Relat. Mater.* **11**, 686–691 (2002).

55. Oliveira, F. S., Cipriano, R. B., da Silva, F. T., Romão, E. C. & dos Santos, C. A. M. Simple analytical method for determining electrical resistivity and sheet resistance using the van der Pauw procedure. *Sci. Rep.* **10**, 1–8 (2020).

56. Cook, T. E. *et al.* Band offset measurements of the GaN (0001)/HfO 2 interface. *J. Appl. Phys.* **94**, 7155–7158 (2003).

57. Perfetti, P. The problem of heterojunction band discontinuities. *Surf. Sci.* **189**–**190**, 362–372 (1987).

58. Lo Nigro, R., Schilirò, E., Mannino, G., Di Franco, S. & Roccaforte, F. Comparison between thermal and plasma enhanced atomic layer deposition processes for the growth of HfO2 dielectric layers. *J. Cryst. Growth* **539**, 125624 (2020).

59. Li, Y. *et al.* Trap characteristics of hafnium oxide-based ferroelectric field-effect transistors measured by using a current transient method. *Appl. Phys. Lett.* **122**, (2023).

60. Boris, D. R. *et al.* The role of plasma in plasma-enhanced atomic layer deposition of crystalline films. *J. Vac. Sci. Technol. A Vacuum, Surfaces, Film.* **38**, (2020).

61. Peter James King-University of Liverpool, Hafnium oxide-based dielectrics by atomic layer deposition. (2013).

APPENDIX A

COPYRIGHT PERMISSION

Copyright permission for the re-use/re-print of the following figures was obtained or requested from the publishers. The detailed permission agreement for each figure or table copyright statements in the text can be provided upon request. Please contact me at avdeshm3@asu.edu if there is any copyright violation in this dissertation.

A. No Permission Agreement Required for the Following Figures:

Figure 0.1: © Kevin G Crawford, Isha Maini, David A. Macdonald, David A.J Moran. Published by Elsevier

Figure 0.2: © Kevin G Crawford, Isha Maini, David A. Macdonald, David A.J Moran. Published by Elsevier